



4-2014

Electron Capture by Multiply Charged Ions from Molecular Targets

Justin Harris
Western Michigan University

Follow this and additional works at: https://scholarworks.wmich.edu/masters_theses

 Part of the Atomic, Molecular and Optical Physics Commons

Recommended Citation

Harris, Justin, "Electron Capture by Multiply Charged Ions from Molecular Targets" (2014). *Masters Theses*. 473.

https://scholarworks.wmich.edu/masters_theses/473

This Masters Thesis-Open Access is brought to you for free and open access by the Graduate College at ScholarWorks at WMU. It has been accepted for inclusion in Masters Theses by an authorized administrator of ScholarWorks at WMU. For more information, please contact wmu-scholarworks@wmich.edu.



**ELECTRON CAPTURE BY MULTIPLY CHARGED IONS FROM
MOLECULAR TARGETS**

by
Justin Harris

A thesis submitted to the Graduate College
in partial fulfillment of the requirements for
the degree of Master of Arts
Physics
Western Michigan University
April 2014

Thesis Committee:

Emanuel Kamber, Ph.D., Chair
Ahsgar Kayani, Ph.D.
Dean Halderson, Ph.D.

ELECTRON CAPTURE BY MULTIPLY CHARGED IONS FROM MOLECULAR TARGETS

Justin Harris, M.A.

Western Michigan University, 2014

State-selective differential cross sections for single-electron capture processes in collisions of Ne^{q+} ($q=2, 3, 5$) ions with H_2O and CO_2 have been studied experimentally at laboratory collision energies between 45 and 250 eV, and at scattering angles between 0° and 7.20° by means of translational energy-gain spectroscopy technique. The translational energy spectra show that only a few final states are populated depending on the projectile's charge state, laboratory scattering angle, and the collision energy. In addition, these measurements show that the dominant reaction channels are due to non-dissociative electron capture into excited states of the projectile product $\text{Ne}^{(q-1)+}$. Contributions from capture accompanied by the excitation of the target product are also observed. Furthermore, reaction channels have been observed which indicate the presence of the long-lived metastable states of Ne^{2+} in the incident beam. The energy-gain spectra are qualitatively interpreted in terms of the reaction windows, which are calculated using the single-crossing Landau-Zener model (LZ) and the extended version of the classical over barrier model (ECOB). The energy dependence of cross sections for single-electron capture by Ne^{2+} ions from H_2O and CO_2 are also measured and are found to slowly increase with the collision energy.

Declaration of Authorship

I, Justin Harris, declare that this thesis titled, 'Electron Capture by Multiply Charged Ions from Molecular Targets' and the work presented in it are my own. I confirm that:

- This work was done wholly or mainly while in candidature for a graduate degree at this University.
- Where any part of this thesis has previously been submitted for a degree or any other qualification at this University or any other institution, this has been clearly stated.
- Where I have quoted from the work of others, the source is always given. With the exception of such quotations, this thesis is entirely my own work.
- I have acknowledged all main sources of help.
- Where the thesis is based on work done by myself jointly with others, I have made clear exactly what was done by others and what I have contributed myself.

Signed:

Date:

Acknowledgements

I would like to express my gratitude to my adviser Dr. Emanuel Kamber for his guidance during the course of this study. Most importantly, I'd like to explicitly thank him for his encouragement and support throughout my time with him at WMU.

I would like to thank the committee members, Dr. Asghar Kayani and Dr. Dean Halderson, for their comments and reviews of this thesis.

I wish to thank Dr. Asghar Kayani for all of his efforts at the WMU accelerator laboratory, Additionally, I'd like to thank Alan Kern and Rick Welch for their work in the accelerator laboratory and metal shop.

Finally, I would like to thank my wife and children for their sacrifices and encouragement in my physics studies.

Justin Harris

Contents

Declaration of Authorship	i
Acknowledgements	ii
List of Figures	v
List of Tables	vi
Abbreviations	vii
1 Introduction	1
1.1 Electron Capture	1
1.1.1 Previous Research	2
1.2 In this Thesis	2
2 Theoretical Background	4
2.1 Ion-Molecule Collisions	4
2.1.1 Single Electron Capture and Transfer Excitation	4
2.1.2 Kinematics	5
2.2 Theoretical Models	6
2.2.1 Landau-Zener Model	7
2.2.2 Classical Over-Barrier Model	9
2.3 Classical Differential Cross Section	11
2.4 Critical Angle	11
2.5 Reaction Window	12
3 Experimental Procedure	13
3.1 Experimental Apparatus	13
3.1.1 Differential Energy-Gain Spectrometer	16
3.1.2 Recoil-Ion Source	17
3.1.3 Electrostatic Analyzer	17
4 Data Analysis	19
4.1 Charge-State Spectroscopy	19

4.2	Energy Analysis	20
5	Results and Discussion	29
5.1	Translational Energy-Gain Spectra	29
5.1.1	Ne ²⁺ - CO ₂ Collisions	29
5.1.2	Ne ²⁺ - H ₂ O Collisions	31
5.1.3	Ne ³⁺ - H ₂ O Collisions	32
5.1.4	Ne ³⁺ - CO ₂ Collisions	33
5.1.5	Ne ⁵⁺ - H ₂ O Collisions	34
5.2	Differential Cross-Sections	35
5.3	Total Cross-Sections	36
6	Conclusion	38
	Bibliography	39

List of Figures

2.1	Potential Curves of SEC	6
3.1	WMU Van de Graaff Accelerator	14
3.2	SNICS	15
3.3	Experimental set-up	16
3.4	Electronic Block Diagram	18
4.1	Charge State Spectrum	20
4.2	Channel Calibration	21
4.3	Channel Calibration with Slope F	22
5.1	Translational Energy-Gain Spectra $Ne^{2+} - CO_2$	30
5.2	Translational Energy-Gain Spectra $Ne^{2+} - H_2O$	31
5.3	Translational energy-gain spectra for 75 eV $Ne^{3+} - H_2O$ collisions	32
5.4	Translational energy-gain spectrum $Ne^{3+} - CO_2$	33
5.5	Translational energy-gain spectrum $Ne^{5+} - H_2O$	34
5.6	Differential Cross Section $Ne^{3+} - H_2O$	35
5.7	Ne^{2+} Cross Section	36

List of Tables

4.1	Single-Electron Capture reaction channels for $Ne^{2+} + H_2O$ Collisions . . .	24
4.2	Single-Electron Capture reaction channels for $Ne^{2+} + CO_2$ Collisions . . .	25
4.3	Single-Electron Capture reaction channels for $Ne^{3+} + H_2O$ Collisions . . .	26
4.4	Single-Electron Capture reaction channels for $Ne^{3+} + CO_2$ Collisions . . .	27
4.5	Single-Electron Capture reaction channels for $Ne^{5+} + H_2O$ Collisions . . .	28

Abbreviations

SEC	Single Electron Capture
DEC	Double Electron Capture
MEC	Multi Electron Capture
LZ	Landau-Zener (theoretical model)
COB	Classical Over-Barrier (theoretical model)
ECOB	Extended Classical Over-Barrier (theoretical model)
SNICS	Sputtering Negative Ion Cesium Source
ESA	Electrostatic Analyzer
MCP	Micro-Channel Plates
PSA	Position-Sensitive Anode
FWHM	Full Width at Half Maximum

Chapter 1

Introduction

1.1 Electron Capture

Among the principal topics for research in atomic physics is the study of collisions involving atomic and molecular particles. Three fundamental atomic processes may occur as a result of ion-atom collisions: excitation, ionization, and electron capture. Of particular interest is single-electron capture from neutral target molecules by multiply-charged ions because this is the predominant reaction for low energy collisions. When low-energy multiply-charged ions collide with molecular targets, electron capture may occur through a variety of reaction channels, including; single-electron capture (SEC), multi-electron capture (MEC), electron capture with accompanying target excitation or ionization, and electron capture with simultaneous projectile excitation.

The reasons for studying electron capture processes in ion-molecule collisions include laser development, astrophysical plasmas, and potential applications in techniques of mass spectrometry in medical research and drug development [1]. In particular, Neon is frequently introduced in Tokamak¹ devices as a diagnostic element for fusion plasmas. In addition to any technological applications and development the research may provide, it is important to have a growing body of data for low-energy collisions of multiply-charged ions with neutral molecular targets to both test the existing theoretical models of atomic structure and to help in the development of more-and-more realistic theoretical models. It is the importance of carbon dioxide and water molecules in fundamental researches for Physics and Chemistry, as well as potential use in applied fields

¹A type of magnetic confinement device, and is one of the most-researched candidates for producing controlled thermonuclear fusion power

like plasma environments and astrophysics that has prompted this study of ion-molecule collisions of Ne ions with CO_2 and H_2O targets.

1.1.1 Previous Research

There has been considerable attention devoted to SEC by multiply-charged ions from neutral targets in the past two decades [2–10]. More specifically, measurements of SEC by multiply-charged Ne ions from atomic and molecular targets have been reported by several investigators [2, 6, 10, 11]. By analyzing outgoing projectiles with coinciding target ions they have made measurements for the cross sections of direct ionization, electron capture, and transfer ionization. However, despite the growing body of experimental and theoretical research in the field, there is still very much to be learned about electron capture and other related processes in low-energy ion-molecule collisions.

In recent years, considerable efforts have been directed towards the study of interaction between multiply charged ions present in solar winds and neutral gases abundant in the earth’s atmosphere. Measurements have been made of the total cross sections for single-electron capture in collisions of Ne^{2+} with N_2 , CO_2 and H_2O at impact energies between 50 and 400 eV and also for single-, double-, and triple-electron capture in collisions of Ne^{6+} ions with CO_2 and H_2O at energies between 450 and 2400 eV [2, 10].

1.2 In this Thesis

The scope of this dissertation is to present the experimental work that measured the translational energy-gain spectra and differential cross sections for single-electron capture in collisions of Ne^{q+} ($q=2, 3, 5$) with H_2O and CO_2 at impact energies between 45 eV and 250 eV and scattering angles between 0° and 7.20° . A differential energy gain spectrometer—capable of simultaneously measuring the scattering angle and energy spectrum of the capturing projectile—is used to obtain measurements on state-selective non-dissociative electron capture of low-energy multiply-charged neon ions in collisions with molecular targets. The measurements of the energy gain spectra are compared with the reaction window predicted by the single-crossing Landau-Zener (LZ) and extended version of the classical-over-the-barrier (ECOB) theoretical models. The energy dependence of cross-sections for single-electron capture by Ne^{2+} ions from H_2O and CO_2

are also measured and compared with the predictions of multi-channel LZ and ECOB calculations.

In the next chapter, the theoretical background for modeling ion-atom collisions is discussed. The experimental procedure and apparatus are described in Chapter 3, followed by a discussion of the data analysis techniques and the experimental results, with comparison to previous studies and theoretical predictions in Chapter 4. Finally, Chapter 5 gives conclusion to the considerations of this thesis.

Chapter 2

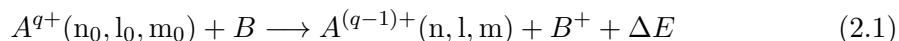
Theoretical Background

2.1 Ion-Molecule Collisions

The focus of this chapter is the theoretical models used to study single-electron capture by multiply charged ions from target molecules at sufficiently low collision energies. Emphasis will be placed on those models which are related to the prediction of the final state populations of the captured electrons, differential, and total cross sections for single-electron capture.

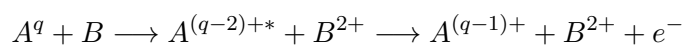
2.1.1 Single Electron Capture and Transfer Excitation

Single-electron capture (SEC) is the most probable process in low-energy multiply charged ion-molecule collisions [10]. This collision may be represented by the equation



where q is the initial charge state of the projectile ion A , ΔE is the energy defect of the reaction, and (n_0, l_0, m_0) and (n, l, m) are the respective quantum numbers of the initial and final states of the projectile ion.

Besides SEC, transfer ionization is also significant in some collision systems. Transfer ionization is the process where double-electron capture occurs to doubly excited states followed by the loss of one projectile electron via autoionization and may be represented by,



Because the projectile ion has a charge state changed by one unit after a transfer ionization event, it can appear as SEC under charge state analysis.

2.1.2 Kinematics

In a classical two-body collision, the translational energy (E) of an ion following an inelastic scattering process differs from the projectile ion energy (E_0) by

$$Q = E - E_0 = \Delta E - \Delta K \quad (2.2)$$

where ΔK is the translational energy given to the target, ΔE is the energy defect of the reaction, and Q is the total change in internal energy that takes place during the inelastic collision. The change in internal energy Q , typically called the ‘‘Q-value’’ of the reaction, can be negative or positive depending on the binding energy of the captured electron and plays a central role in the experimental evaluation of electron capture in ion-atom collisions. The energy defect ΔE is calculated according to the formula

$$\Delta E = I_p(A^{(q-1)+}) - I_p(B) - E_x \quad (2.3)$$

where $I_p(A^{(q-1)+})$ and $I_p(B)$ are the ionization potentials of the projectile product ion $A^{(q-1)+}$ and the target atom B , and E_x is the excitation energy of the x th level of the projectile product ion $A^{(q-1)+}$ or target product ion B^+ .

The translational energy ΔK that is given to the target may be calculated with the formula

$$\Delta K = \frac{m_p}{m_p + M} (1 - \cos \theta_p) \left(\frac{2ME_0}{m_p + M} - \Delta E \right) + \frac{m_p(\Delta E)^2}{4ME_0} \cos \theta_p \quad (2.4)$$

where θ_p is the laboratory scattering angle of the projectile, m_p is the projectile mass, and M is the target mass [12]. However, for these collision systems, values of ΔK calculated on the basis of zero scattering angles are found to be small. Therefore eq. (2.2) reduces to $Q = \Delta E$ [10]. In this thesis, the translational energy-gain spectra are expressed in terms of the Q-values and no correction was added to the measured energy gain.

2.2 Theoretical Models

In the process of electron capture by ion-molecule collisions with multiply-charged ion from neutral molecular target, the products of the collision will have positive charges and the interaction between them is repulsive. However, before the collision event, the ion-atom interaction is of an attractive nature that is relatively weak at large internuclear separation. Because of this, electron capture in ion-molecule collisions is considered a typical example of an interaction which can proceed through curve-crossing. According to the curve-crossing picture of electron capture, the transition from initial state to final state occurs near the curve crossing point of molecular potential energy curves corresponding to different separated-atom states, also called *incoming* ($A^{+z}+B$) and *outgoing* ($A^{z-1^*}+B^+$) channels (fig. 2.1).

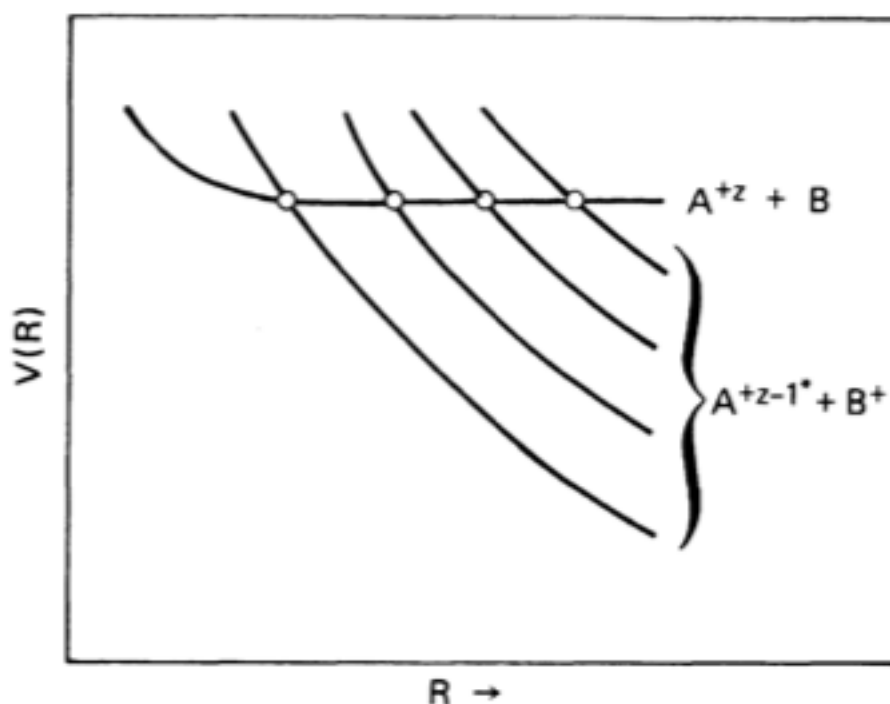


FIGURE 2.1: Schematic diagram for the potential curves of the electron transfer reaction: $A^{q+} + B \rightarrow A^{(q-1)+} + B^+$

2.2.1 Landau-Zener Model

The earliest theoretical work on curve-crossing was done by Landau and Zener, who both derived the well-known formula for the transition probability independently. This theoretical model is known today as the Landau-Zener model (LZ) of transition probability. In the LZ model, the transition from initial state to final state is assumed to occur at the crossing point of a pair of diabatic potential energy curves corresponding to ingoing ($A^{q+} + B$) and outgoing ($A^{(q-1)+} + B^+$) channels where the single-crossing probability at each crossing point R_x is given by,

$$P_n = \exp \left[\frac{-2\pi(H_{12})^2}{\mathbf{v}_r \Delta F} \right] \quad (2.5)$$

where H_{12} is the coupling matrix element approximately equal to half the adiabatic splitting at the curve crossing R_x , ΔF is the difference in slopes of the diabatic potential curves at the curve-crossing, and \mathbf{v}_r is the radial velocity; also at the curve-crossing [13].

If one assumes a repulsive Coulomb interaction $V_1(R)$ in the outgoing channel and zero interaction $V_2(R)$ in the incoming channel, the potential curve slope difference ΔF can be re-written as the differential of the interaction potentials with respect to R and evaluated at $R - R_x$. That is,

$$\Delta F = \left. \frac{d}{dR} [V_1(R) - V_2(R)] \right|_{R=R_x} \cong \frac{q-1}{R^2} \quad (2.6)$$

where q is the charge state of the incident ion.

In the straight-line trajectory approximation, the radial velocity \mathbf{v}_r at the curve-crossing R_x can be written,

$$\mathbf{v}_r = v_0 \left[1 - \left(\frac{b}{R_x} \right)^2 \right]^{\frac{1}{2}} \quad (2.7)$$

where b is the impact parameter and v_0 is the relative velocity [14]. As usual, the most difficult problem is in developing a formulation for the coupling matrix that can be easily applied from case to case.

One method for expressing the coupling matrix elements was developed by Olson and Salop for collisions of fully-ionized ions with hydrogen atoms. By obtaining the matrix elements H_{12} for a large number of stripped-ion-atomic-hydrogen systems from

analysis of pseudocrossings observed in the exact adiabatic potential curves using the OEDM program of J. D. Power, Olson and Salop arrived at the reduced parameters

$$H_{12}^* = \sqrt{q}H_{12}$$

and

$$R_x^* = \frac{R_x}{\sqrt{q}}$$

where all quantities are in atomic units [15, 16].

Generalizing their results to systems where the target is not atomic hydrogen Olson and Salop were able to conclude with the expression,

$$H_{12}^* = (9.13)\sqrt{q} e^{(1.324\alpha R_x^*)} \quad (2.8)$$

where R_x^* is the reduced parameter listed above, $\alpha = \sqrt{I_t(\text{eV})/13.6}$, and I_t is the ionization potential of the target atom. In atomic units this becomes simply $\alpha = \sqrt{2I_t(\text{a.u.})}$. The coefficient of this coupling matrix was reduced by Kimura et al. to 5.48 (from 9.13) in order to reach good agreement with measurements of their studies [14].

There are two possible ways in which electron capture occurs in the crossing point of potential energy curves; capture can occur on the way *in* to a collision or on the way *out* of a collision. The probability of electron transfer for each curve is $P = p(1 - p)$, where p is the probability that the system will remain on the same potential curve when crossing, and $(1 - p)$ is the probability for a jump from one curve to the other curve. Therefore, when combined with the possibility of capture both *in* to and *out* of a collision, the total probability of electron transfer for two states at a single crossing for a given impact parameter is,

$$P = 2p(1 - p) \quad (2.9)$$

By applying Olson and Salop's extension of the LZ model to multichannel systems (figure 2.1) with probability $P_n(n = 1, 2, \dots, n)$, we can calculate the probability of capture in the n th final state. Assuming that there is no interference between different

paths leading to a particular final state, the n th final state capture probability is

$$\begin{aligned}
P_n = & p_2 p_3 \dots p_n (1 - p_n) [1 + (p_{n+1} p_{n+2} \dots p_N)^2 \\
& + (p_{n+1} p_{n+2} \dots p_{N-1})^2 (1 - p_N)^2 \\
& + (p_{n+1} p_{n+2} \dots p_{N-2})^2 (1 - p_{N-1})^2 \\
& + \dots + p_{n+1}^2 (1 - p_{n+2})^2 + (1 - p_{n+1})^2]
\end{aligned} \tag{2.10}$$

For the case of partially-stripped projectiles, a correction term has been suggested for H_{12} [17]. The correction term is dependent on the quantum numbers n and l of the transferred electron's final capture state and is given by the expression,

$$f_{nl} = \frac{(-1)^{n+1-l} \sqrt{2l+1} \Gamma(n)}{\sqrt{\Gamma(n+1+l) \Gamma(n-1)}} \tag{2.11}$$

The addition of this correction term to the coupling matrix element gives it the form,

$$H_{12}^* = f_{nl} (9.13) \sqrt{q} e^{(1.324 \alpha R_x^*)} \tag{2.12}$$

The cross section (σ_n) for capture into a particular final state n is given in terms of the impact parameter b and crossing distance R_x by

$$\sigma_n = 2\pi \int_0^{R_x} P_n b db \tag{2.13}$$

with P_n as the probability for capture in the the n th final state.

2.2.2 Classical Over-Barrier Model

The classical over-barrier model (COB) and extended classical over-barrier model (ECOB) is applicable to multiply charged ion-atom collisions in the low keV range of impact energies. It has been used extensively to calculate cross sections for single-electron capture processes and to identify the main capture channels. The model describes collisions of the type:



That is, an ion-atom collision between an ion of $q+$ charge and neutral target atom (or molecule), in which r electrons are transferred from the target atom to the projectile [18]. The COB model is based on the idea that electrons can transition from the target to the projectile at such internuclear distances that the “height” of the potential barrier between the target and projectile is lower than the binding energy of the electrons.

Due to the Coulomb field of the ion the energy levels of the target electrons will Stark shift and become stronger bound,

$$E_i(R) = E_{b,i} - \frac{q}{R} \quad (2.15)$$

where R is the internuclear distance and $E_{b,i}$ is the binding energy of the i th target electron.¹ The potential experienced by the i th electron is the potential of the approaching ion added to that of its own nucleus

$$V_i^{\text{in}}(r) = -\frac{q}{|\mathbf{R} - \mathbf{r}|} - \frac{i}{|\mathbf{r}|} \quad (2.16)$$

for $0 < |\mathbf{r}| < |\mathbf{R}|$, where \mathbf{r} is the coordinate of the i th electron with respect to the parent nucleus. The ion-atom potential well “height” depends on the internuclear distance. At the distance in which the potential well height is equal to the Stark shifted binding energy, the electron can escape the target potential. For the i th electron, this distance (the capture radius) is given by:

$$R_i^{\text{in}} = \frac{2\sqrt{iq} + 1}{-E_{b,i}} = \frac{2\sqrt{iq} + 1}{|I_{p,i}|} \quad (2.17)$$

At this distance, the i th electron is no longer localized on the target and moves in the joint potential well of the target and the projectile. The COB model further assumes that the shifted binding energy on the way in remains fixed, i.e., $E_i(R) = E_i(R_i^{\text{in}})$ for $R \leq R_i^{\text{in}}$. A constraint was later put on the internuclear separation for SEC in the form [19],

$$R_x \leq \frac{(2\sqrt{q} + 1)}{|I_p|} \quad (2.18)$$

and states that the highest value for R_x compatible with both Eq. 2.18 and the following equation for the crossing radius,

$$R_x = \frac{q - 1}{\left(\frac{q^2}{2n^2} - |I_p|\right)} \quad (2.19)$$

¹Note that the binding energy E_b is just opposite in sign of the ionization potential I_p , i.e. $E_b = -I_p$

will define the most probable quantum number n and the R_x to be used to calculate the classical cross section [19].

$$\sigma = \pi R_x^2 \quad (2.20)$$

2.3 Classical Differential Cross Section

The classical differential cross section $\frac{d\sigma}{d\Omega}$, differential with respect to the solid angle Ω , relates the incoming intensity of the particles to the number of particles scattered into an element of solid angle $d\Omega$, in the direction specified by the scattering angle Θ . The relationship between the impact parameter b and the deflection angle $\Theta(b)$ of the projectile ion in the center-of-mass coordinate is given by Goldstein,

$$\Theta = \pi - \oint \frac{b|dr|}{r^2 \sqrt{(1 - \frac{V(r)}{E_{cm}} - \frac{b^2}{r^2})}} \quad (2.21)$$

Where E_{cm} is the initial kinetic energy of the projectile's center of mass, $V(r)$ is the scattering potential, and r is the internuclear separation.

Integration of Eq. 2.21 for any impact parameter b yields the classical deflection angle $\Theta(b)$ as a function of the impact parameter, which can be transformed to a scattering angle in the laboratory setting and compared with experimental results. The differential cross section for scattering into the solid angle $d\Omega$ is obtained from this $\Theta(b)$ and given by [?],

$$\frac{d\sigma}{d\Omega} = \frac{b}{\sin \Theta} \left| \frac{db}{d\Theta} \right| \quad (2.22)$$

2.4 Critical Angle

As discussed in the Landau-Zener Model of section 2.2, for a two-state system, there are two possible paths that the system can follow for electron capture, resulting in a double-branching of the angular deflection $\Theta(b)$. The upper branch of the deflection function corresponds to the projectile trajectory followed by capture on the way *in*, while the lower branch corresponds to the trajectory followed by capture on the way *out*. The two branches meet at a critical angle Θ_c which corresponds to capture at an impact parameter equal to the crossing radius R_x . On the basis of the semi-classical two-state scattering model, the critical angle Θ_c has been estimated by assuming that capture occurs at a localized curve crossing between the potential energy curves for the

entrance and exit channels [20]. For small scattering angles in the laboratory frame, the critical angle is given by,

$$\Theta_c = \frac{Q}{2E_0} \quad (2.23)$$

where Q is the energy gain of the reaction channel and E_0 is the initial kinetic energy of the projectile. This angle separates the events at smaller angles due to capture on the way out; and events at larger angles due to capture on the way in.

At smaller internuclear distances, inside the crossing radius there are usually exit channels with a Q -value higher than the dominant exit channel which behave adiabatically at the entrance channel crossing. Therefore, the entrance channel is not flat but has a repulsive potential energy curve inside the active crossing. This causes the lower branch of the deflection function to rise at small angles, producing a maximum in the differential cross section—that is, the differential cross section is asymptotic—at a scattering angle Θ_r . This angle Θ_r , corresponding to the small angle for which two impact parameters result in the same scattering angle.

2.5 Reaction Window

The important curve crossings between the diabatic potential energy curves associated with the entrance channel and various exit channels are those which occur at moderate internuclear separations, where the probability for single-electron capture is large. This intermediate range of separations is commonly referred to as the reaction window for the electron capture process. The position of the reaction window for any collision system depends mainly on the collision energy of the projectile. When the collision energy is reduced the adiabaticity at inner crossings becomes increasingly pronounced, while the transition probability at distant crossings becomes larger. Therefore, the reaction window shifts toward larger internuclear separations if the collision energy is reduced and vice versa. Several authors have calculated the location of the reaction window as a function of the crossing radius [7, 9, 14, 21].

Chapter 3

Experimental Procedure

In this chapter we describe the production of the fluorine ion beam from the tandem accelerator, the electrostatic analyzer (ESA), and our procedure for data acquisition.

3.1 Experimental Apparatus

A general schematic of the WMU tandem Van de Graaff accelerator is shown in fig 3.1. This accelerator facility has two negative ion sources: a direct extraction negative ion-exchange source and a sputtering cesium negative ion source (SNICS) (fig 3.2), which produces negative ions from solids. The SNICS source was used to produce a fluorine ion beam for the work described here. Inside the SNICS, the cesium oven is heated so that the cesium vapor flows into the ion source. After cesium atoms are ionized by contact with the hot tungsten coil, they are attracted to the CaF_2 packed sputter cathode and held at negative 6 kV with respect to the ionizer. The energetic cesium ions sputter atoms from the surface of the cathode.

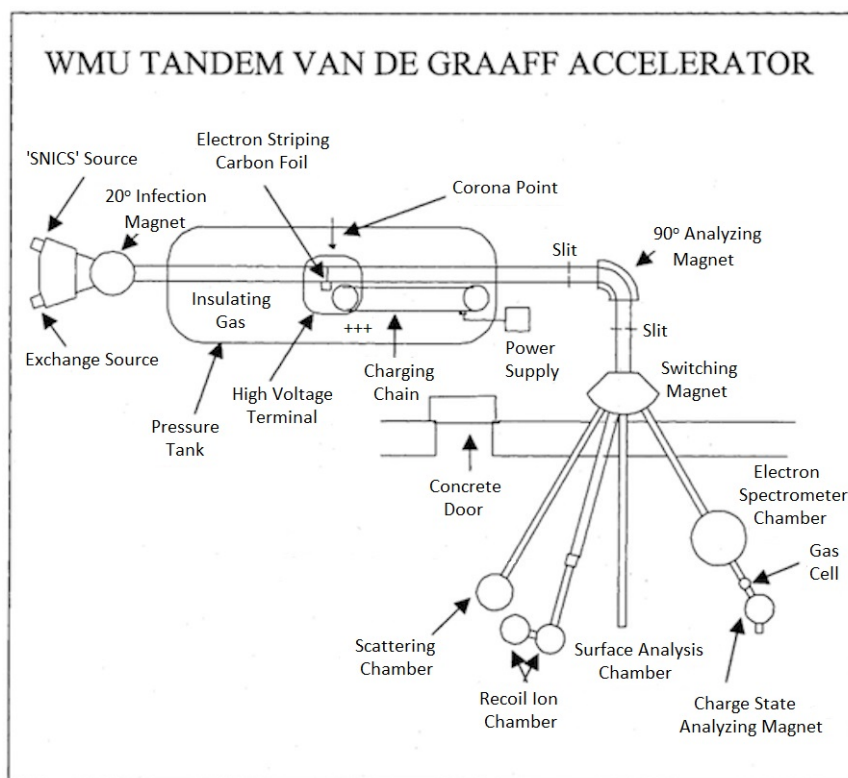


FIGURE 3.1: Schematic drawing of the Western Michigan University tandem Van de Graaff accelerator and associated beam lines

A number of these sputtered fluorine atoms collide with cesium atoms near the cathode where they capture an electron and become negative ions. These ions are repelled by the cathode and accelerated towards an extraction electrode with an acceleration voltage of negative 13 kV towards a final focus electrode and pre-acceleration tube. Negative Fluorine ions ($q = -1$) are analyzed by a 20° inflection magnet and focused by an einzel lens into the low energy end of the accelerator tube. Since this accelerator is a tandem accelerator, the negative ions are accelerated towards the positive terminal voltage, which is set at approximately 4 MV, where electrons are stripped off by a low density oxygen gas and the ions become positively charged ions. These ions are then repelled by the positive terminal voltage and accelerated a second time, gaining a total kinetic energy of $(q+1)V$, where V is the positive voltage on the terminal and $q=1, 2, 3, \dots$ is the charge state of the positive ions emerging from the stripper gas.

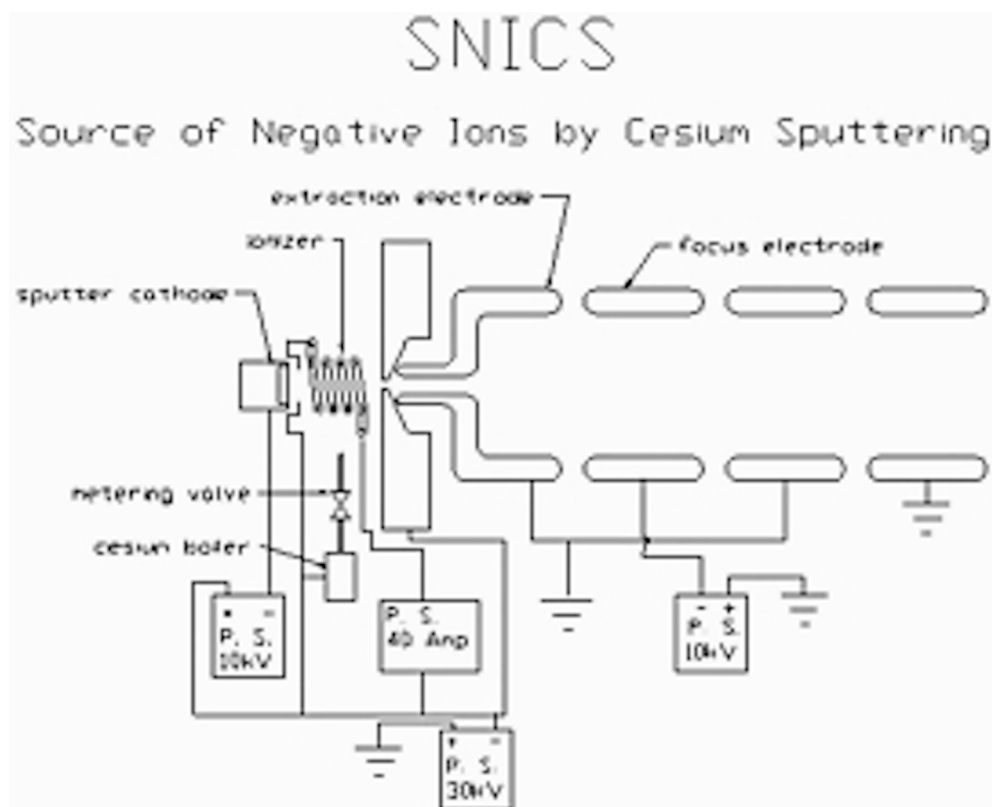


FIGURE 3.2: Schematic drawing of the SNICS ion source at the WMU tandem Van de Graaff Accelerator facility

After the beam leaves the high-energy end of the accelerator, it is focused on a set of defining slits to form an object for the analyzing magnet. The analyzing magnet bends the beam through a 90° angle and forms an image at the second set of slits. The strength of the field in the analyzing magnet is set to select the energy and the charge state of the ions that will reach the target. The currents produced by the portion of the beam striking the image slits is converted into a signal which can also be fed back to the corona system to stabilize the terminal voltage. Finally, the ion beam is directed into the target room through the selected atomic physics beam line by way of a switching magnet. The selected beam is collimated by a set of four-jaw slits and guided to the recoil ion source, where doubly charged Neon ions are produced. For convenient tuning of the ion current, a small Faraday cup (located behind the recoil ion source) was used. Typical currents collected by the Faraday cup were between 0.5 and 1 μA .

3.1.1 Differential Energy-Gain Spectrometer

The differential energy-gain spectrometer described here was used to study low energy electron capture processes. The experimental apparatus, shown in fig 3.3 consists of a recoil ion source, analyzing magnet, deflecting plates, target collision cell, electrostatic analyzer, and detector.

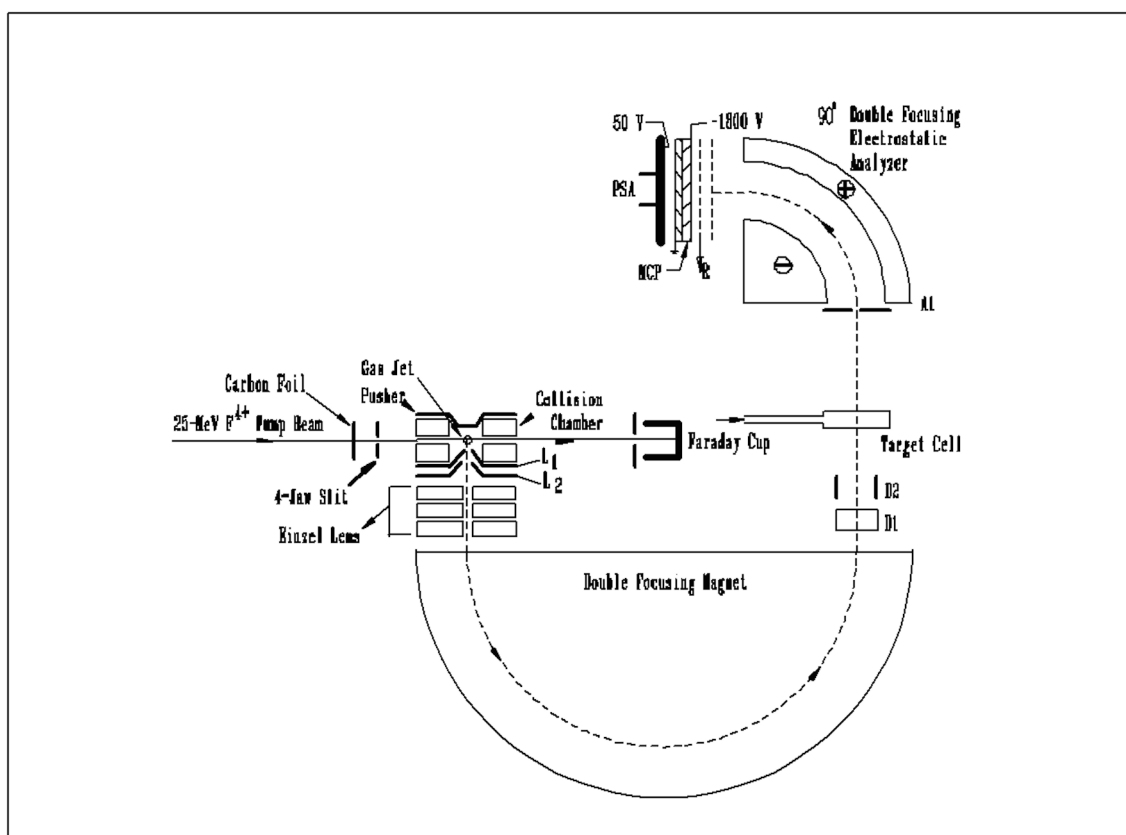


FIGURE 3.3: Schematic drawing of the experimental apparatus showing the recoil ion source, double focusing magnet, target cell, electrostatic analyzers, channeltrons, and channel plate detector

3.1.2 Recoil-Ion Source

The recoil-ion source is made up of a collision chamber, a pusher, gas nozzle, and two lenses (L_1 and L_2). The Neon gas atoms flowed into the source through a 3 cm long copper nozzle with an inside diameter of 120 μm , which was placed at the center between the pusher and L_1 . The gas pressure in the recoil ion source was adjusted until the pressure of the main chamber was raised to $\sim 3.5 \times 10^{-7}$ Torr.

A beam of 25 MeV F^{4+} was collected by a Faraday cup after it passed through the collision chamber, which has entrance and exit apertures of 2.5 mm and 3 mm in diameter, respectively. Slow recoil Neon ions formed in the ion source were extracted perpendicular to the pump beam with an acceleration voltage V_{acc} , which is equal to the voltage applied on the pusher, through a 2.5 mm diameter aperture in L_1 and 4mm aperture in L_2 , under the influence of a potential field set up by positive voltages imposed to the pusher and lenses L_1 and L_2 . The recoil ion beam extracted from the recoil source was focused by an einzel lens into the entrance aperture of a 180° double-focusing analyzing magnet of radius 11.5 cm, where mass-to-charge selection of the ions was accomplished. Following momentum analysis, the ion beam was guided with the aid of horizontal and vertical parallel deflection plates into the entrance of a 5.56 mm-long collision cell with entrance and exit aperture diameters of 1mm and 2mm, respectively. The projectile ions scattered through a nominal angle Θ into a solid angle ($\Delta\Omega$) of approximately 3×10^{-3} sr were energy analyzed by a 90° double-focusing electrostatic analyzer (ESA). The collision cell pressure was monitored by a capacitance nanometer (MKS Baratron), and was typically ≤ 2 mtorr, to ensure single-collision conditions.

3.1.3 Electrostatic Analyzer

The scattering angle Θ is controlled by an aperture (1mm in diameter) in front of the ESA, ions were then detected by a one-dimensional position-sensitive micro-channel plate detector, which is located at the focal plane of the ESA. The detector device consists of two 3.5 cm diameter micro-channel plates (MCP) and a one-dimensional position-sensitive anode encoder (PSA). The potential across each plate was maintained at approximately -900 V, for a total of approximately -1800 V across the entire configuration. The output electrons generated by the MCPs were accelerated towards and

collected by the PSA. The charge gathered by the PSA was used to determine the position of events along a single dimension. Electrodes on either side of the resistive anode collect fractions of the total charge deposited.

The relative position of an event is determined by the ratio between the resulting voltage pulse at one electrode and the sum of the voltage pulses of both electrodes, that is

$$X = \frac{V_L}{V_U + V_L} \quad (3.1)$$

Here, X is the relative position along the PSA axis and V_U and V_L are the voltage pulse heights at the upper and lower electrodes, respectively.

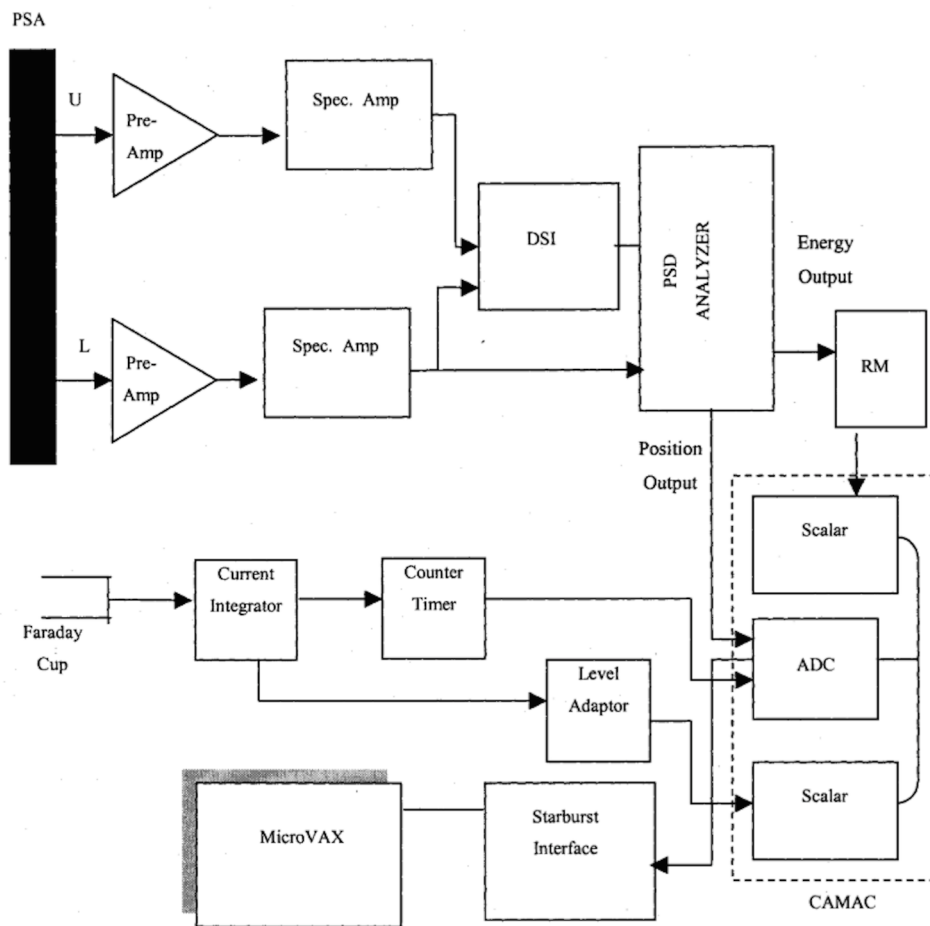


FIGURE 3.4: Electronic block diagram for angular distribution measurements.

Chapter 4

Data Analysis

In this chapter, we describe the procedure used to obtain the charge state spectrum for the recoil ions produced in the recoil ion source and the translational energy-gain spectra for SEC by Ne^{q+} ions from H_2O and CO_2 measured at a range of scattering angles and impact energies.

4.1 Charge-State Spectroscopy

The ability to analyze the ion beam produced in the recoil ion source requires that the different charge components be separated and focused into discrete beams so that their intensities can be measured. This is accomplished by a magnetic field placed in a direction perpendicular to the direction of the ion motion. The individual beams are then collected and plotted into a charge state spectrum (fig. 4.1) , where the charge state of each peak in the spectrum is identified by plotting the square root of the mass-to-charge ratio vs. the magnet current for each peak, resulting in a linear relation that is used to identify each charge state.

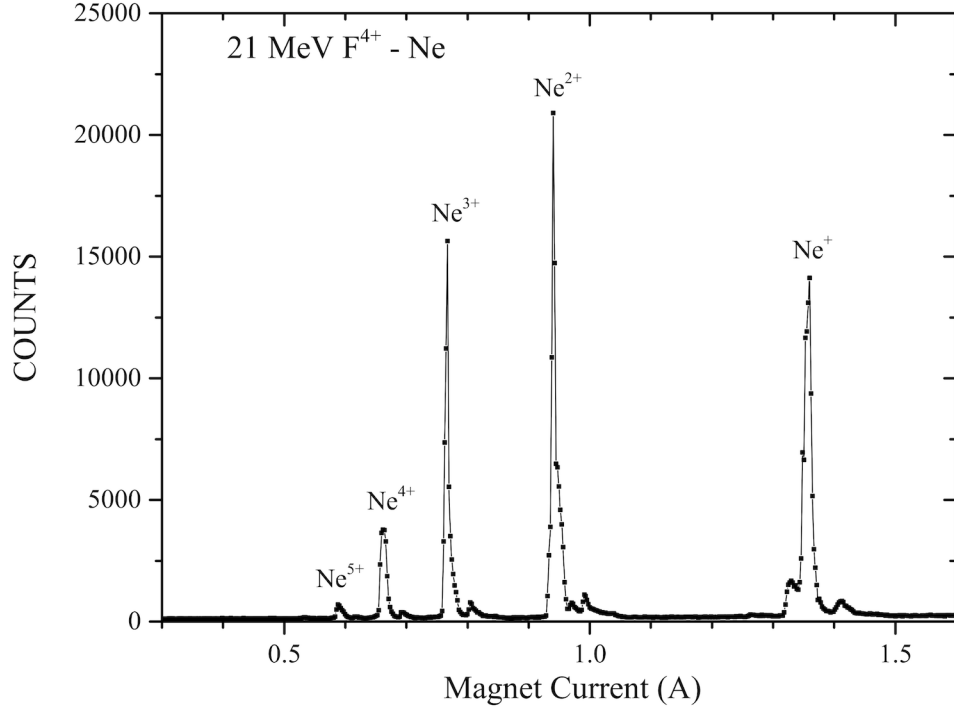


FIGURE 4.1: Charge state spectrum for recoil neon ions produced in the recoil ion source.

4.2 Energy Analysis

The energy gain Q of the projectile following SEC is calculated in terms of the relation between acceleration voltage V_{acc} and the voltage applied across the electrostatic analyzer via the expression [20],

$$Q = \left[\left(\frac{q'V}{qV_o} \right) - 1 \right] qV_{acc} \quad (4.1)$$

where V_o and V are the applied voltage to the analyzer (either the DFA or PPA) for which the primary beam and ions undergoing capture are passed, respectively, and q & q' are the charge state of the projectile before and after the collision, respectively.

However, in the case of DFA, the energy gain Q can be expressed in terms of the projectile peak position as follows [20],

$$Q(x) = \left[\frac{(S(0) - S(x))}{(FV_o - S(0) + S(x))} \right] qV_{acc} \quad (4.2)$$

in which $S(0)$ and $S(x)$ are the positions of the main peak of the exchanged projectile and product ions, respectively, and F is the slope of the projectile peak position plotted as a function of DFA voltage.

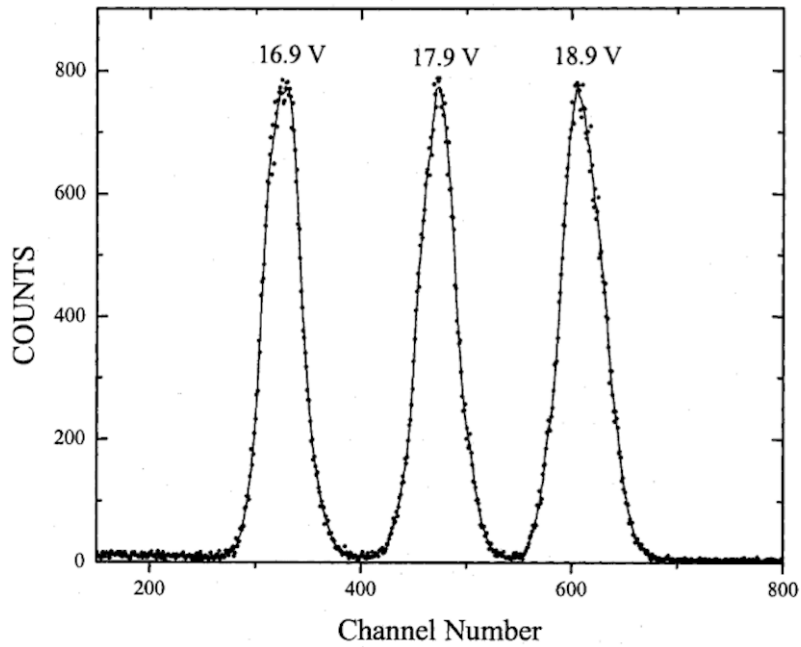


FIGURE 4.2: Projectile peaks corresponding to channel number as a function of the DFA voltages

Figure 4.2 shows an example plot of projectile peaks as a function of DFA voltage, where the peaks are plotted with respect to channel number. The slope F is then the average distance, in channel numbers, between projectile peaks (fig. 4.3)

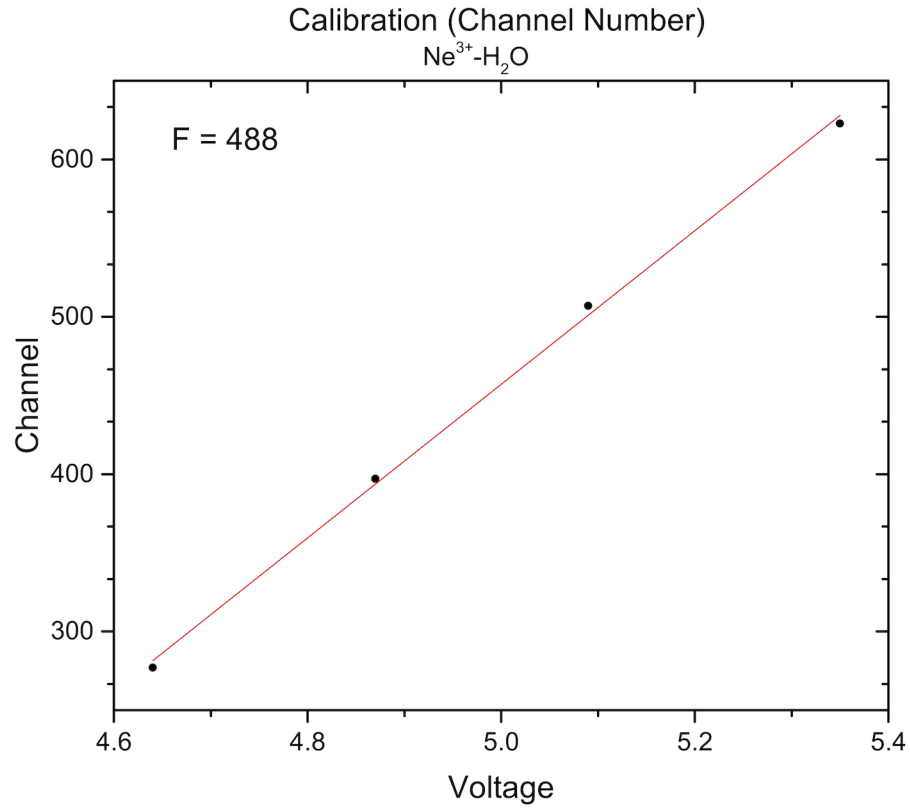


FIGURE 4.3: Typical channel number calibration with a slope of $F=488$ for $Ne^{3+}-H_2O$ collisions

For convenience and comparison, we identify the reaction channels following SEC by three letters, typically of the form $I\alpha X$, according to the notation previously used by Kamber et al. [2, 10]. The designations I, II, and III represent the ground and metastable states of the incident ion, respectively, with $\alpha, \beta, \gamma, \dots$ representing the ground and successively higher excited states of the projectile product, respectively. The designations X, A, B, \dots represent the ground state and higher excited states of the target product, whereas Y represents target double ionization. The possible outgoing channels following electron capture are listed in tables 4.2 - 4.5. The energy levels used in calculating the energy-defects were taken from Bashkin and Stoner, the NIST atomic spectra database, and—for molecular targets—from photo-electron spectroscopy data [22, 23]. The energies ΔE were calculated assuming that the projectile ion is in

its ground state or metastable states, and molecular targets & their products are at the lowest vibrational levels ($\nu = 0$). For molecular targets, the energy defects have been calculated assuming the ionization energies of the target are those for vertical processes.

TABLE 4.1: Single-Electron Capture reaction channels for $Ne^{2+} + H_2O$ Collisions

Reactant and Initial State	Product and Final State	ΔE (eV)	Designation of Reaction
$Ne^{2+} (2s^2 2p^4 \ ^3P) + H_2O(X \ ^1\Sigma_1^+)$	$\rightarrow Ne^+ (2s^2 p^5 \ ^2P) + H_2O^+(X \ ^1\Sigma_1^+)$	28.46	I α X
	$\rightarrow Ne^+ (2s^2 p^6 \ ^2S)$	1.55	I β X
	$\rightarrow Ne^+ (2s^2 p^4 ({}^3P) 3s \ ^4P)$	1.39	I γ X
	$\rightarrow Ne^+ (2s^2 p^4 ({}^3P) 3s \ ^2P)$	0.68	I δ X
	$\rightarrow Ne^+ (2s^2 p^4 ({}^3P) 3p \ ^4P)$	-2.06	I ϵ X
	$\rightarrow Ne^+ (2s^2 p^4 ({}^1D) 3s \ ^2D)$	-2.09	I ζ X
	$\rightarrow Ne^+ (2s^2 p^4 ({}^3P) 3p \ ^4D)$	-2.42	I η X
	$\rightarrow Ne^+ (2s^2 p^4 ({}^3P) 3p \ ^2P)$	-3.05	I θ X
	$\rightarrow Ne^+ (2s^2 p^4 ({}^3P) 3s \ ^2F)$	-5.55	I ι X
	$\rightarrow Ne^+ (2s^2 p^5 \ ^2P) + H_2O^+(X \ ^1\Sigma_1^+)$	31.66	II α X
	$\rightarrow Ne^+ (2s^2 p^5 \ ^2P)$	5.20	II α Y
	$\rightarrow Ne^+ (2s^2 p^6 \ ^2S)$	4.75	II β X
	$\rightarrow Ne^+ (2s^2 p^4 ({}^3P) 3s \ ^4P)$	4.59	II γ X
	$\rightarrow Ne^+ (2s^2 p^4 ({}^3P) 3s \ ^2P)$	3.88	II δ X
	$\rightarrow Ne^+ (2s^2 p^4 ({}^3P) 3p \ ^4P)$	1.14	II ϵ X
$\rightarrow Ne^+ (2s^2 p^4 ({}^1D) 3s \ ^2D)$	1.11	II ζ X	
$\rightarrow Ne^+ (2s^2 p^4 ({}^3P) 3p \ ^4D)$	1.01	II η X	
$\rightarrow Ne^+ (2s^2 p^4 ({}^3P) 3p \ ^2P)$	0.63	II θ X	
$\rightarrow Ne^+ (2s^2 p^4 ({}^3P) 3s \ ^2F)$	-2.35	II ι X	
$Ne^{2+} (2s^2 2p^4 \ ^1S) + H_2O(X \ ^1\Sigma_1^+)$	$\rightarrow Ne^+ (2s^2 p^5 \ ^2P) + H_2O^+(X \ ^1\Sigma_1^+)$	35.37	III α X
	$\rightarrow Ne^+ (2s^2 p^6 \ ^2S)$	8.46	III β X
	$\rightarrow Ne^+ (2s^2 p^4 ({}^3P) 3s \ ^4P)$	8.30	III γ X
	$\rightarrow Ne^+ (2s^2 p^4 ({}^3P) 3s \ ^2P)$	7.59	III δ X
	$\rightarrow Ne^+ (2s^2 p^4 ({}^3P) 3s \ ^2P) + H_2O^+(\tilde{A} \ ^2A_1)$	6.35	III δ A
	$\rightarrow Ne^+ (2s^2 p^4 ({}^3P) 3p \ ^4P)$	4.85	III ϵ X
	$\rightarrow Ne^+ (2s^2 p^4 ({}^1D) 3s \ ^2D)$	4.72	III ζ X
	$\rightarrow Ne^+ (2s^2 p^4 ({}^3P) 3p \ ^4D)$	4.34	III η X
	$\rightarrow Ne^+ (2s^2 p^4 ({}^3P) 3p \ ^2P)$	3.86	III θ X
	$\rightarrow Ne^+ (2s^2 p^4 ({}^3P) 3s \ ^2F)$	1.36	III ι X

TABLE 4.2: Single-Electron Capture reaction channels for $Ne^{2+} + CO_2$ Collisions

Reactant and Initial State	Product and Final State	ΔE (eV)	Designation of Reaction	
$Ne^{2+} (2s^2 2p^4 \ ^3P) + CO_2(X \ ^1\Sigma_g^+)$	$\rightarrow Ne^+ (2s2p^5 \ ^2P) + CO_2^+(X \ \Sigma_g^+)$	27.30	I α X	
	$\rightarrow Ne^+ (2s2p^6 \ ^2S)$	0.39	I β X	
	$\rightarrow Ne^+ (2s2p^4(^3P)3s \ ^4P)$	0.13	I γ X	
	$\rightarrow Ne^+ (2s2p^4(^3P)3s \ ^2P)$	-0.48	I δ X	
	$\rightarrow Ne^+ (2s2p^4(^3P)3p \ ^4P)$	-3.22	I ϵ X	
	$\rightarrow Ne^+ (2s2p^4(^1D)3s \ ^2D)$	-3.25	I ζ X	
	$\rightarrow Ne^+ (2s2p^4(^3P)3p \ ^4D)$	-3.58	I η X	
	$\rightarrow Ne^+ (2s2p^4(^3P)3p \ ^2P)$	-4.21	I θ X	
	$\rightarrow Ne^+ (2s2p^4(^3P)3s \ ^2F)$	-6.71	I ι X	
	$Ne^{2+} (2s^2 2p^4 \ ^1D) + CO_2(X \ ^1\Sigma_g^+)$	$\rightarrow Ne^+ (2s2p^5 \ ^2P) + CO_2^+(X \ \Sigma_g^+)$	30.50	II α X
		$\rightarrow Ne^+ (2s2p^5 \ ^2P)$	5.39	II α Y
		$\rightarrow Ne^+ (2s2p^6 \ ^2S)$	3.59	II β X
		$\rightarrow Ne^+ (2s2p^4(^3P)3s \ ^4P)$	3.33	II γ X
		$\rightarrow Ne^+ (2s2p^4(^3P)3s \ ^2P)$	2.72	II δ X
$\rightarrow Ne^+ (2s2p^4(^3P)3p \ ^4P)$		-0.02	II ϵ X	
$\rightarrow Ne^+ (2s2p^4(^1D)3s \ ^2D)$		-0.05	II ζ X	
$\rightarrow Ne^+ (2s2p^4(^3P)3p \ ^4D)$		-0.38	II η X	
$\rightarrow Ne^+ (2s2p^4(^3P)3p \ ^2P)$		-1.01	II θ X	
$\rightarrow Ne^+ (2s2p^4(^3P)3s \ ^2F)$		-3.51	II ι X	
$Ne^{2+} (2s^2 2p^4 \ ^1S) + CO_2(X \ ^1\Sigma_g^+)$		$\rightarrow Ne^+ (2s2p^5 \ ^2P) + CO_2^+(X \ \Sigma_g^+)$	34.22	III α X
		$\rightarrow Ne^+ (2s2p^6 \ ^2S)$	7.31	III β X
		$\rightarrow Ne^+ (2s2p^4(^3P)3s \ ^4P)$	7.05	III γ X
		$\rightarrow Ne^+ (2s2p^4(^3P)3s \ ^2P)$	6.44	III δ X
	$\rightarrow Ne^+ (2s2p^4(^3P)3p \ ^4P)$	3.70	III ϵ X	
	$\rightarrow Ne^+ (2s2p^4(^1D)3s \ ^2D)$	3.67	III ζ X	
	$\rightarrow Ne^+ (2s2p^4(^3P)3p \ ^4D)$	3.34	III η X	
	$\rightarrow Ne^+ (2s2p^4(^3P)3p \ ^2P)$	2.71	III θ X	
	$\rightarrow Ne^+ (2s2p^4(^3P)3s \ ^2F)$	0.21	III ι X	

TABLE 4.3: Single-Electron Capture reaction channels for $Ne^{3+} + H_2O$ Collisions

Reactant and Initial State	Product and Final State	ΔE (eV)
$Ne^{3+} (2s^2 2p^3 \ ^4S) + H_2O(X \ ^1\Sigma_1^+)$	$\rightarrow Ne^{2+} (2s^2 2p^4 \ ^3P) + H_2O^+(X \ ^1\Sigma_1^+)$	50.81
	$\rightarrow Ne^{2+} (2s^2 2p^4 \ ^1D)$	47.60
	$\rightarrow Ne^{2+} (2s^2 2p^4 \ ^1S)$	43.89
	$\rightarrow Ne^{2+} (2s 2p^5 \ ^3P)$	25.48
	$\rightarrow Ne^{2+} (2s 2p^5 \ ^1P)$	14.91
	$\rightarrow Ne^{2+} (2s^2 2p^3 \ (^4S) 3s \ ^3S)$	11.20
	$\rightarrow Ne^{2+} (2s^2 2p^3 \ (^4S) 3p \ ^5P)$	7.61
	$\rightarrow Ne^{2+} (2s^2 2p^3 \ (^2D) 3s \ ^3D)$	7.02
	$\rightarrow Ne^{2+} (2s^2 2p^3 \ (^4S) 3p \ ^3P) + H_2O^+(A \ ^2A_1)$	6.57
	$\rightarrow Ne^{2+} (2s^2 2p^3 \ (^2D) 3s \ ^1D)$	4.58
	$\rightarrow Ne^{2+} (2s^2 2p^3 \ (^2P) 3s \ ^3P)$	4.37
	$\rightarrow Ne^{2+} (2s^2 2p^3 \ (^2P) 3s \ ^1P)$	3.71
	$\rightarrow Ne^{2+} (2s^2 2p^3 \ (^2D) 3p \ ^1P)$	2.70

TABLE 4.4: Single-Electron Capture reaction channels for $Ne^{3+} + CO_2$ Collisions

Reactant and Initial State	Product and Final State	ΔE (eV)
$Ne^{3+} (2s^2 2p^3 \ ^4S) + CO_2(X \ ^1\Sigma_g^+)$	$\rightarrow Ne^{2+} (2s^2 2p^4 \ ^3P) + CO_2^+(X \ \Sigma_g^+)$	49.65
	$\rightarrow Ne^{2+} (2s^2 2p^4 \ ^1D)$	46.44
	$\rightarrow Ne^{2+} (2s^2 2p^4 \ ^1S)$	42.74
	$\rightarrow Ne^{2+} (2s 2p^5 \ ^3P)$	24.21
	$\rightarrow Ne^{2+} (2s 2p^5 \ ^1P)$	13.76
	$\rightarrow Ne^{2+} (2s^2 2p^3(^4S) 3s \ ^3S) + CO_2^+(A \ ^3\Pi_u)$	10.05
	$\rightarrow Ne^{2+} (2s^2 2p^3(^4S) 3p \ ^5P)$	6.45
	$\rightarrow Ne^{2+} (2s^2 2p^3(^2D) 3s \ ^3D)$	5.86
	$\rightarrow Ne^{2+} (2s^2 2p^3(^4S) 3p \ ^3P)$	5.42
	$\rightarrow Ne^{2+} (2s^2 2p^3(^2D) 3s \ ^1D)$	5.27
	$\rightarrow Ne^{2+} (2s^2 2p^3(^2P) 3s \ ^3P)$	3.22
	$\rightarrow Ne^{2+} (2s^2 2p^3(^2P) 3s \ ^1P)$	2.56
	$\rightarrow Ne^{2+} (2s^2 2p^3(^2D) 3p \ ^1P)$	1.55

TABLE 4.5: Single-Electron Capture reaction channels for $Ne^{5+} + H_2O$ Collisions

Reactant and Initial State	Product and Final State	ΔE (eV)
$Ne^{5+} (2p^2 P) + H_2O(X^1 \Sigma_1^+)$	$\longrightarrow Ne^{4+} (2s^2 2p 3d^1 D) + H_2O^+(X^2 B_1)$	27.16
	$\longrightarrow Ne^{4+} (2s 2p^2 ({}^4 P) 3s^5 P)$	27.05
	$\longrightarrow Ne^{4+} (2s^2 2p 3d^3 D)$	26.59
	$\longrightarrow Ne^{4+} (2s^2 2p 3d^3 P)$	25.62
	$\longrightarrow Ne^{4+} (2s^2 2p 3d^1 F)$	25.48
	$\longrightarrow Ne^{4+} (2s^2 2p 3d^1 P)$	24.43
	$\longrightarrow Ne^{4+} (2s 2p^2 ({}^4 P) 3s^3 P)$	22.24
	$\longrightarrow Ne^{4+} (2s 2p^2 ({}^4 P) 3p^3 S)$	21.55
	$\longrightarrow Ne^{4+} (2s 2p^2 ({}^4 P) 3p^5 D)$	20.98
	$\longrightarrow Ne^{4+} (2s 2p^2 ({}^4 P) 3p^5 P)$	19.61
	$\longrightarrow Ne^{4+} (2s 2p^2 ({}^4 P) 3p^3 D)$	19.44
	$\longrightarrow Ne^{4+} (2s 2p^2 ({}^4 P) 3p^5 S)$	18.70
	$\longrightarrow Ne^{4+} (2s 2p^2 ({}^4 P) 3p^3 P)$	17.17
	$\longrightarrow Ne^{4+} (2s 2p^2 ({}^2 D) 3s^3 D)$	15.80
	$\longrightarrow Ne^{4+} (2s 2p^2 ({}^4 P) 3d^5 F)$	14.99
	$\longrightarrow Ne^{4+} (2s 2p^2 ({}^4 P) 3d^5 D)$	14.60
	$\longrightarrow Ne^{4+} (2s 2p^2 ({}^4 P) 3d^5 P)$	14.29
	$\longrightarrow Ne^{4+} (2s 2p^2 ({}^4 P) 3d^3 P)$	14.14
	$\longrightarrow Ne^{4+} (2s^2 2p 4s^3 P)$	13.80
	$\longrightarrow Ne^{4+} (2s^2 2p 4s^1 P)$	13.69
	$\longrightarrow Ne^{4+} (2s 2p^2 ({}^4 P) 3d^3 F)$	12.43
	$\longrightarrow Ne^{4+} (2s 2p^2 ({}^4 P) 3d^3 D)$	12.38
	$\longrightarrow Ne^{4+} (2s^2 2p 4p^1 P)$	11.82
	$\longrightarrow Ne^{4+} (2s^2 2p 4p^3 D)$	11.40
	$\longrightarrow Ne^{4+} (2s^2 2p 4p^3 P)$	11.35
	$\longrightarrow Ne^{4+} (2s 2p^2 ({}^2 D) 3p^1 D)$	10.80
	$\longrightarrow Ne^{4+} (2s 2p^2 ({}^2 D) 3p^1 F)$	10.16
	$\longrightarrow Ne^{4+} (2s 2p^2 ({}^2 D) 3p^1 P)$	9.72
	$\longrightarrow Ne^{4+} (2s^2 2p 4d^3 F)$	9.32
	$\longrightarrow Ne^{4+} (2s^2 2p 4d^1 F)$	9.17
	$\longrightarrow Ne^{4+} (2s^2 2p 4d^3 D)$	8.95
	$\longrightarrow Ne^{4+} (2s^2 2p 4d^3 P)$	8.92
	$\longrightarrow Ne^{4+} (2s^2 2p 4f^1 F)$	8.74
	$\longrightarrow Ne^{4+} (2s^2 2p 4f^3 F)$	8.73
	$\longrightarrow Ne^{4+} (2s^2 2p 4f^3 G)$	8.69
	$\longrightarrow Ne^{4+} (2s^2 2p 4d^1 P)$	8.63
	$\longrightarrow Ne^{4+} (2s^2 2p 4d^1 F)$	8.62
	$\longrightarrow Ne^{4+} (2s^2 2p 4f^3 D)$	8.56
	$\longrightarrow Ne^{4+} (2s^2 2p 4f^3 S)$	5.75
	$\longrightarrow Ne^{4+} (2s^2 2p 4f^1 D)$	4.95

Chapter 5

Results and Discussion

5.1 Translational Energy-Gain Spectra

In this chapter, measurements for single-electron capture processes in collisions of Ne^{2+} ions with CO_2 & H_2O molecular targets and Ne^{3+} and Ne^{5+} ions with H_2O molecular targets are presented and discussed. The measurements are classified according to translational energy-gain spectra, differential cross sections, and energy-dependent total cross sections.

5.1.1 Ne^{2+} - CO_2 Collisions

Figure 5.1 shows the translational energy-gain spectrum for single-electron capture (SEC) by 50 eV Ne^{2+} ions from CO_2 at 0° scattering angle. The observed collision spectrum is dominated by a peak due to non-dissociative SEC from the metastable state Ne^{2+} ($2p^4\ ^1S$) ions into the $3s\ ^4P$, $2p^6\ ^2S$, and $3s\ ^2P$ states of Ne^+ with the production of CO_2^+ in the ground state ($X\ \Sigma_g^+$) via reaction channels III γ X, III β X, and III δ X, respectively. Contributions from capture accompanied by the ionization of target product via the reaction channel II α Y cannot be ruled out. The broad peak, centered around $Q = 3$ eV, is due to capture from the metastable state $2p^4\ ^1D$ of Ne^{2+} into the $2p^6\ ^2S$, $3s\ ^4P$, and $3s\ ^2P$ states of Ne^+ via II β X, II γ X, and II δ X channels.

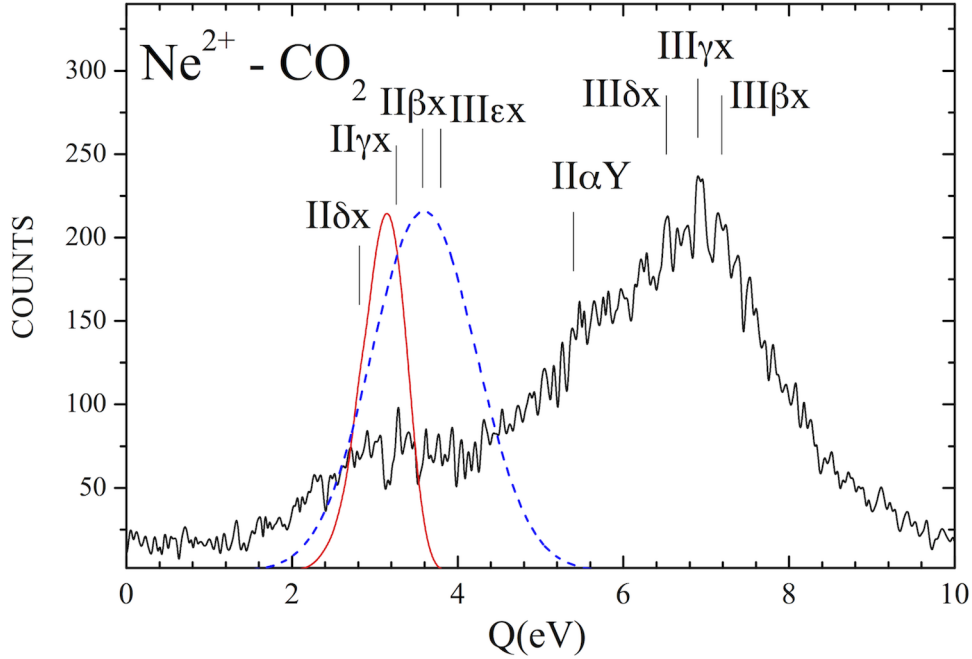


FIGURE 5.1: Translational energy-gain spectra for SEC by 50 eV Ne^{2+} ions from CO_2 at 0° scattering angle. Additionally, the reaction windows predicted by the LZ model (solid line) and ECOB model (dashed line) are shown.

Figure 5.1 also shows our calculated reaction windows using both a single-crossing Landau-Zener (LZ) model and extended classical over-barrier (ECOB) model. Calculated peak values have been normalized to our observed peak values in the translational energy-gain spectrum. The reaction window based on the ECOB model is assumed to be gaussian around the classical value of the minimum Q -value, described by $Q = (q-1)/R_c$, where $R_c = (2\sqrt{q} + 1)/I_p$, q is the charge state of the projectile, and I_p is the ionization potential of the target ion in atomic units, which is related to the time dependence of the potential barrier height, with a width proportional to $v^{1/2}$, where v is the impact velocity of the projectile ions. The reaction window based on a single-crossing LZ model and ECOB model favor reaction channels with smaller Q -values compared to the dominant channels found experimentally.

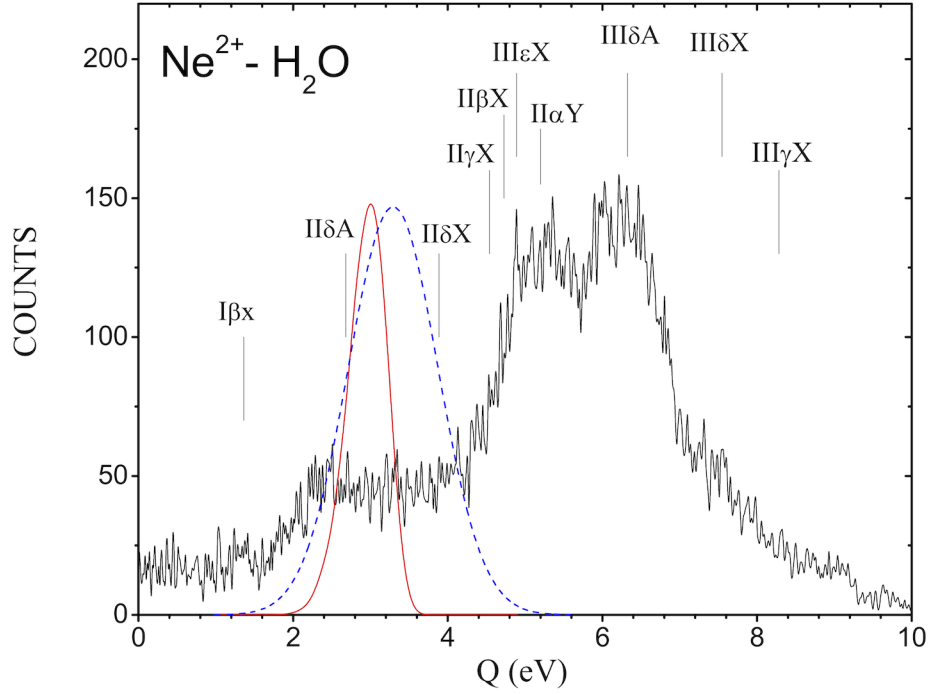
5.1.2 Ne^{2+} - H_2O Collisions

FIGURE 5.2: Translational energy-gain spectra for SEC by 50 eV Ne^{2+} from H_2O at 0° scattering angle. Additionally, the reaction windows predicted by the LZ model (solid line) and ECOB model (dashed line) are shown.

Figure 5.2 shows the translational energy-gain spectrum for SEC by 50 eV collisions of Ne^{2+} ions from H_2O target at 0° scattering angle. The spectrum exhibits three distinct peaks. The most prominent peak (reaction channel III δ A) is due to transfer excitation from the metastable state $2p^4\ ^1S$ of Ne^{2+} ions into the $3s\ ^2P$ state of Ne^+ product ions with production of H_2O^+ into the excited state ($\tilde{A}\ ^2A_1$). The smallest peak at ~ 2.6 eV corresponds to transfer excitation into the $3s\ ^2P$ state of Ne^+ via the reaction channel II δ A. The remaining peak at ~ 5.2 eV is due to capture accompanied by the ionization of the target product (channel II α Y) with contributions from channels III ϵ X and II β X. The reaction windows calculated with the single-crossing LZ model and ECOB model favor Q-values smaller than the observed windows of the dominant channels.

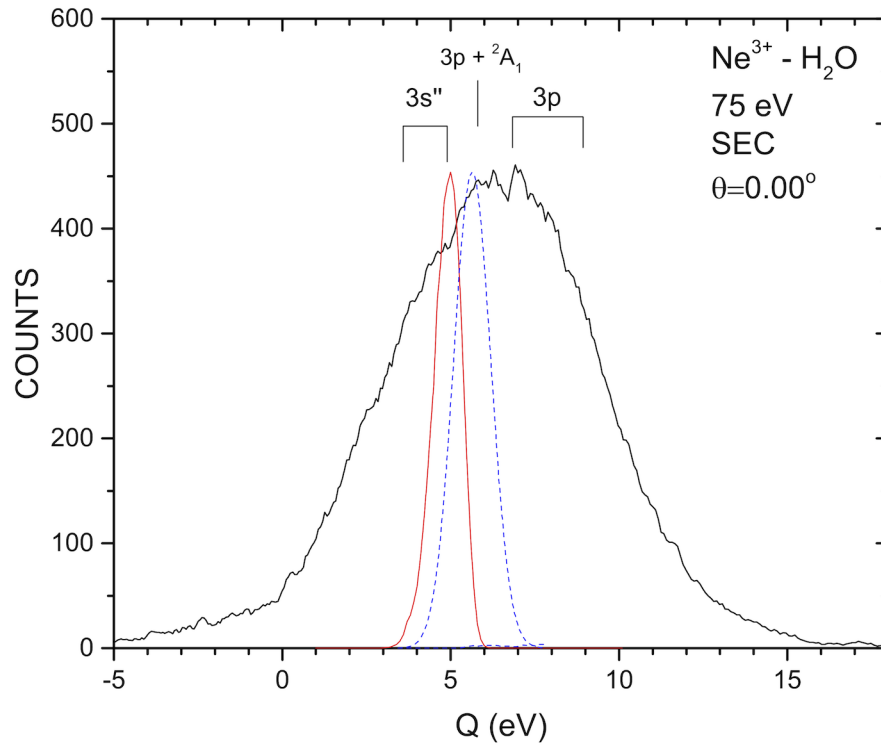
5.1.3 $Ne^{3+} - H_2O$ Collisions

FIGURE 5.3: Translational energy-gain spectrum for 75 eV $Ne^{3+} - H_2O$ collisions at 0° scattering angle. Additionally, the reaction windows predicted by the LZ model (solid line) and ECOB model (dashed line) are shown.

The translational energy-gain spectrum for $Ne^{3+} - H_2O$ collisions at 75 eV is shown in figure 5.3. The spectrum shows a single broad peak at ~ 7.5 eV, corresponding most strongly with capture into the $3p$ states of Ne^{2+} ions, with contributions from transfer excitation into the $3p$ state of Ne^{2+} accompanied by excitation of the target product into the excited state $H_2O^+(\tilde{A}^2A_1)$. There is also some contribution from an unresolved reaction at ~ 4.5 eV corresponding to capture into the $3s''$ states of Ne^{2+}

The reaction window calculated by the LZ model for 75 eV $Ne^{3+} - H_2O$ collisions favors smaller Q -values compared to the dominant channels, with the reaction window calculated by the ECOB model favors transfer excitation as the dominant channel.

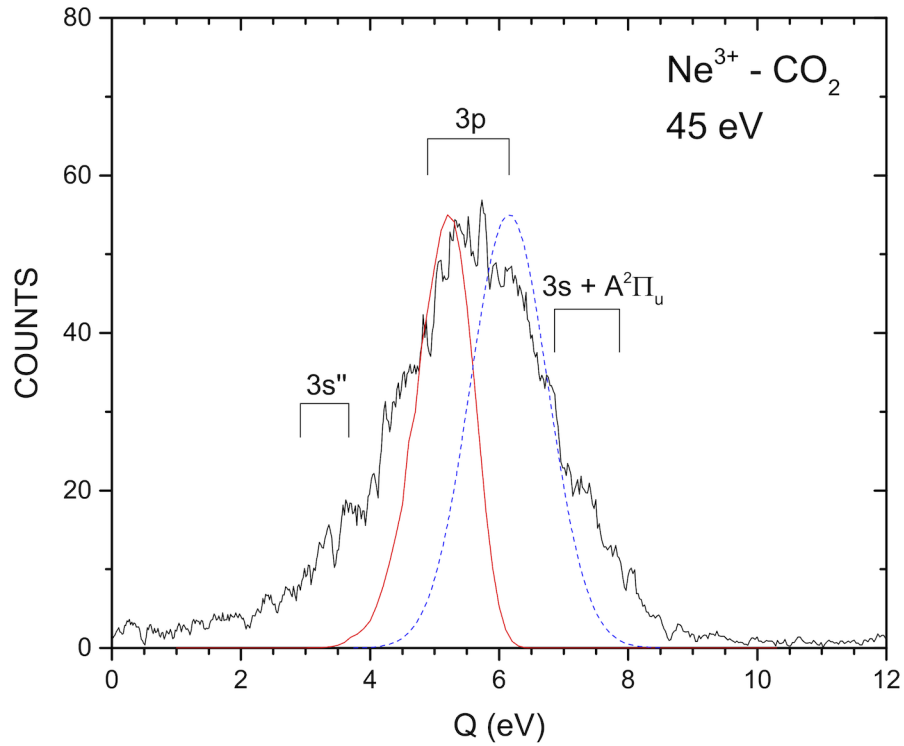
5.1.4 Ne^{3+} - CO_2 Collisions

FIGURE 5.4: Translational energy-gain spectrum for single-electron capture in 45 eV Ne^{3+} - CO_2 collisions. The reaction windows calculated by the LZ model (solid line) and ECOB model (dashed line) are also shown.

Figure 5.4 shows the translational energy-gain spectrum for the formation of Ne^{2+} ions from SEC by 45 eV collisions of Ne^{3+} ions with H_2O at 0° scattering angle. A single dominant peak is seen at ~ 5.5 eV, corresponding to capture into the $3p$ $^{3,5}P$ states of Ne^{2+} with production of CO_2^+ in the ground state ($X \Sigma_g^+$) along with contribution due to transfer excitation into the $3s$ 3S state of Ne^{2+} with production of CO_2^+ in the excited state ($A^2\Pi_u$). The reaction windows predicted by the single-crossing LZ model and ECOB model accommodate the dominant reaction channel and provide the best description of the reaction.

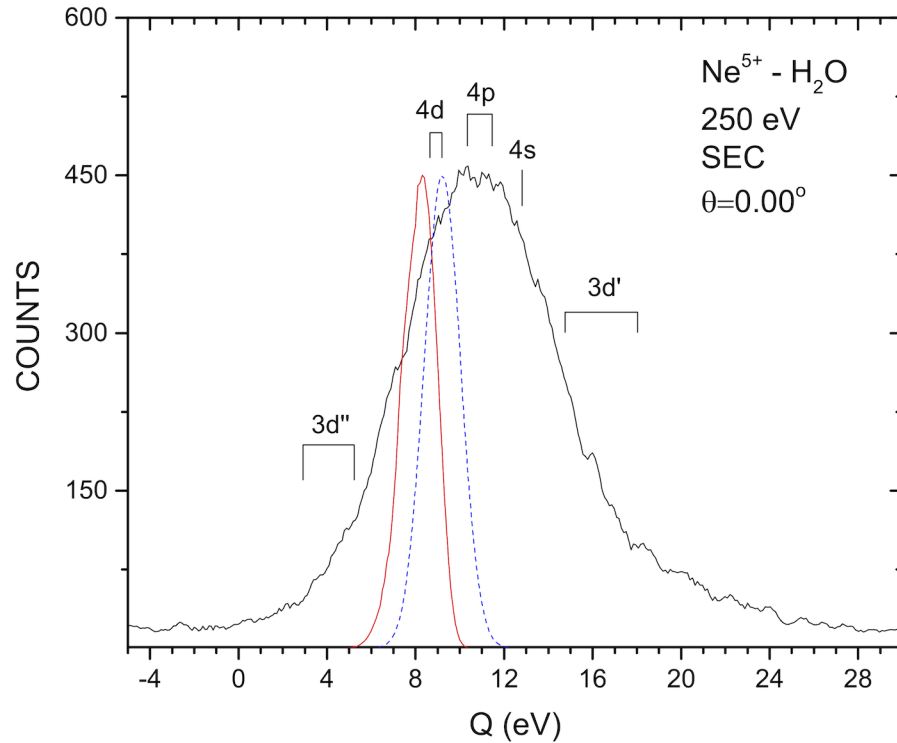
5.1.5 Ne^{5+} - H_2O Collisions

FIGURE 5.5: Translational energy-gain spectrum for SEC by 250 eV Ne^{5+} ions from H_2O at 0° scattering angle. Dominant reaction windows calculated by the LZ model (solid line) and ECOB model (dashed line) are also shown.

Figure 5.5 shows the translational energy-gain spectrum observed for the formation of Ne^{4+} ions from the reaction of 250 eV Ne^{5+} with H_2O at 0° scattering angle. The observed spectrum is dominated by non-dissociative SEC from the ground state incident Ne^{5+} ($2p^2P$) ions into the $4p$ state of Ne^{4+} with production of H_2O^+ in the ground state (X^2B_1), with contributions from capture into $4d$ and $4s$ states. There are also contributions from capture into the $3d''$ and $3d'$ states of Ne^{4+} . The reaction windows calculated by the LZ and ECOB theoretical models favor capture into the $2s^22p\ 4d$ of Ne^{4+} as the dominant reaction channel.

5.2 Differential Cross-Sections

Figure 5.6 shows the differential cross section for SEC by 75 eV Ne^{3+} ions from H_2O . The differential cross sections $\frac{d\sigma}{d\Omega}$ were determined by finding the areas under the peaks in the energy gain spectrum obtained at different projectile laboratory scattering angles. The areas were calculated using a Gaussian curve fitting method through Originlab data analysis software and plotted against the corresponding projectile laboratory scattering angle.

The distribution shows that the projectile products which correlate with the dominant capture channel are distributed forward inside the critical angle ($\theta_c \simeq 2.917^\circ$), corresponding to capture at an impact parameter equal to the crossing radius of the dominant reaction channel. This indicates that capture takes place in these processes on the way out of the collision.

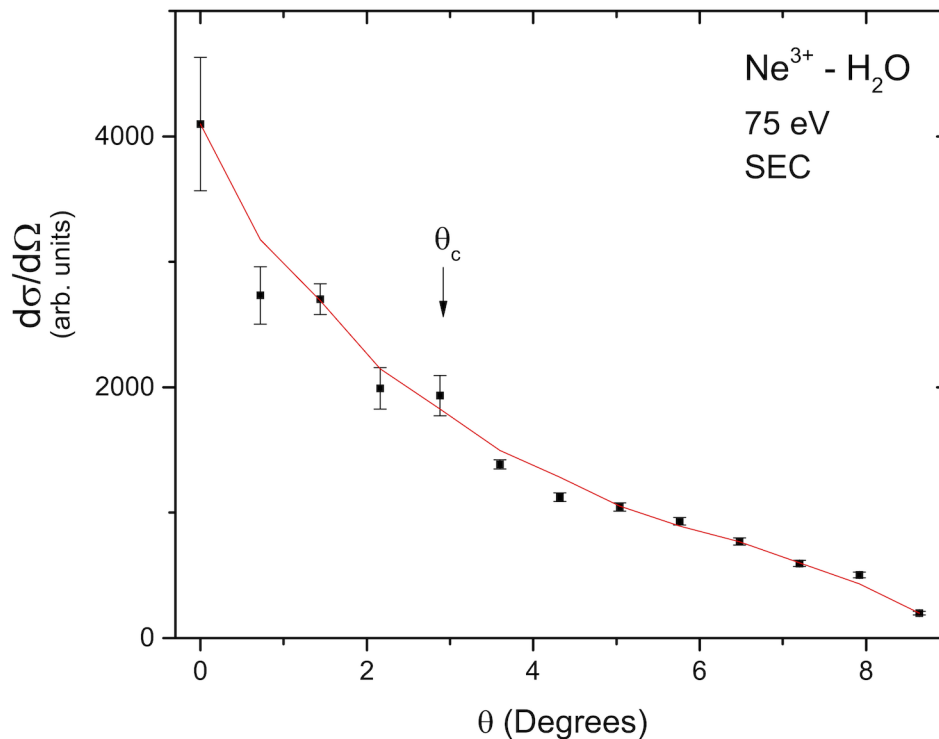


FIGURE 5.6: Experimental differential cross section ($d\sigma/d\Omega$) for SEC of 75 eV Ne^{3+} - H_2O collisions. A smooth line is shown to guide the eye.

5.3 Total Cross-Sections

The measured total cross section for SEC by Ne^{2+} ions from CO_2 and H_2O , together with the LZ and COB theoretical predictions, are shown in figure 5.7. The total experimental uncertainties for absolute values of the total cross sections were obtained by the quadratic sum of the statistical deviations, absolute measurements of target pressures, and detector efficiencies. The absolute uncertainty is estimated to be of the order of $\pm 25\%$ and only relative errors are displayed in the figure.

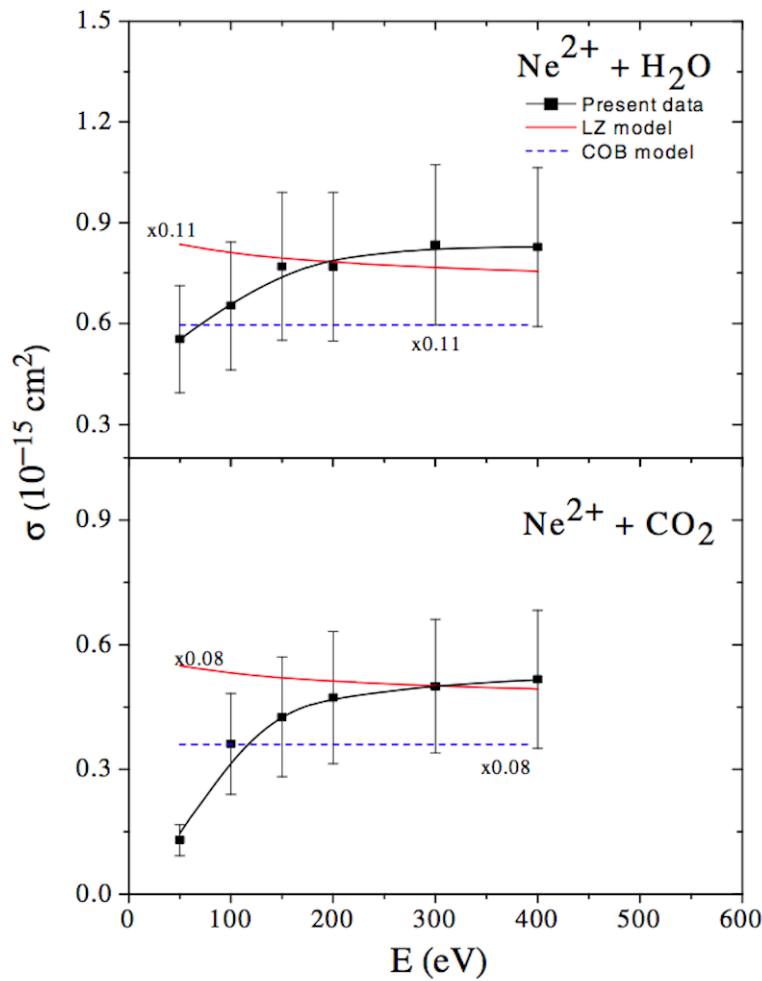


FIGURE 5.7: Measured cross-sections for SEC by Ne^{2+} ions from H_2O and CO_2 . Theoretical calculations and their scaling factors are included.

In both collisions, the total cross sections increase slowly with the collision energy. This can be understood from the reaction window, which gets broader with increasing energy and therefore increases the probability of channels with large Q -values. A full quantum calculation, which requires the consideration of a large number of couplings and curve crossings between the potential energy curves associated with the quasi-molecule formed in the collisions, is not available for comparison, therefore we have relied on the LZ and COB theoretical models for comparison and qualitative explanation of our measurements. As can be seen in figure 5.7, our measured cross sections are at least a factor of 8 to 12 smaller than the theoretical calculations. A possible explanation for this discrepancy could be that the dominant channels are located outside of the reaction windows and are due to the presence of metastable states in the incident beam.

Chapter 6

Conclusion

In this thesis, doubly differential cross sections, in energy and angle, for single electron capture by Ne^{q+} ($q=2, 3, 5$) projectile ions with CO_2 and H_2O molecular targets have been studied by means of translational energy-gain spectroscopy. Measurements were carried out at laboratory impact energies between 45 and 250 eV and at scattering angles between 0° and 7.20° . In addition to non-dissociative single-electron capture channels, we also detected weaker channels due to transfer excitation (i.e., capture accompanied by target excitation), transfer ionization (i.e., capture accompanied by target ionization), and presence of the metastable states Ne^{2+} ($2p^4\ ^1D$ and $\ ^1S$) in the primary beam. In these collision systems, no clear evidence of molecular dissociation was observed. The energy-gain spectra were interpreted qualitatively in terms of the reaction windows, which are calculated using the Landau-Zener (LZ) model and the extended classical over-barrier (ECOB) model. The LZ and ECOB calculations favored Q-values smaller than the dominant channels observed in the Ne^{2+} spectra but compared favorably with the experimental data for Ne^{3+} collisions with H_2O and CO_2 and Ne^{5+} collisions with H_2O . We have also studied differential cross sections for SEC in Ne^{3+} - H_2O collisions. The angular distribution spectra contains a forward peak inside a critical angle θ_c , corresponding to capture at an impact parameter equal to the crossing radius of the dominant reaction channel. The peak is qualitatively explained by a two-state model and is attributed to capture process on the way out of the collision. The energy dependence of cross sections for SEC by Ne^{2+} ions from CO_2 and H_2O were also measured. No data of state-selective SEC by Ne^{2+} from CO_2 and H_2O are, however, available for comparison

Bibliography

- [1] D. M. Meade. *Nucl. Fusion*, 14(289):2, 1974.
- [2] A. Hasan, O. Abu-Haija, T. Elkafrawy, A. Kayani, J. Harris, and E. Y. Kamber. *Physica Scripta*, T156:1–4, 2013.
- [3] J. P. Giese, C. L. Cocke, W. Waggoner, L. N. Tunnell, and S. L. Varghese. *Phys. Rev. A*, 34:3770–3781, 1986.
- [4] E. Y. Kamber, C. L. Cocke, S. Cheng, and S. L. Varghese. *Physical Review Letters*, 60(20):2026–2029, 1988.
- [5] L. R. Andersson, H. Cederquist, A. Bárány, L. Liljeby, C. Biedermann, J. C. Levin, N. Keller, S. B. Elston, J. P. Gibbons, K. Kimura, and I. A. Sellin. *Physical Review A*, 43(7):4075–4078, 1991.
- [6] E. Justiniano, C. L. Cocke, T. J. Gray, R. Dubois, C. Can, W. Waggoner, R. Schuch, H. Schmidt-Böcking, and H. Ingwersen. *Physical Review A*, 29(3):1088–1095, 1984.
- [7] E. Y. Kamber, K. Akgüngör, C. Leather, and A. G. Brenton. *Physical Review A*, 54(2):1452–1458, 1996.
- [8] S. Yaltkaya, E. Y. Kamber, and S. M. Ferguson. *Physical Review A*, 48(1):382–391, 1993.
- [9] O. Abu-Haija, E. Y. Kamber, and D. Mathur. *Chemical Physics Letters*, (408):5–12, 2005.
- [10] O. Abu-Haija, A. Hasan, A. Kayani, and E. Y. Kamber. *EPL*, 93(13003):1–6, 2011.
- [11] L. N. Tunnell, C. L. Cocke, J. P. Giese, E. Y. Kamber, S. L. Varghese, and W. Waggoner. *Physical Review A*, 35(8):3299–3308, 1987.
- [12] Allan Maccoll. *Organic Mass Spectrometry*, 13(12):737–737, 1978.

-
- [13] L. D. Landau. *Phys. Z. Sowjetunion*, 2(46):7, 1932.
- [14] M. Kimura, T. Iwai, Y. Kaneko, N. Kobayashi, A. Matsumoto, S. Ohtani, K. Okuno, S. Takagi, H. Tawara, and S Tsurubuchi. *J. Phys. Soc. Jpn.*, 53(7):2224–2232, 1984.
- [15] J. D. Power. *Phil. Trans. R. Soc. Long. A*, 274:663–697, 1973.
- [16] R. E. Olson and A. Salop. *Physical Review A*, 14(2):579–585, 1976.
- [17] K. Taulbjerg. *J. Phys. B: At. Mol. Opt. Phys.*, 19:367–372, 1986.
- [18] A Niehaus. *Journal of Physics B: Atomic and Molecular Physics*, 19(18):2925, 1986.
- [19] R. Mann, H. F. Beyer, and F. Folkmann. *J. Phys. B: At. Mol. Phys*, 14:1161–1181, 1981.
- [20] L. Cocke, C. Tunnell, W. Waggoner, J. P. Giese, S. M. Varghese, E. Y. Kamber, and J. O. Pedersen. *Nucl. Instrum. Methods in Phys. Res. B*, 97(24), 1987.
- [21] H. Cederquist, H. Andersson, G. Astner, P. Hvelplund, and J. O. P. Pedersen. *Phys. Rev. Lett.*, 62:1465–1468, 1989.
- [22] NIST Atomic Spectroscopy Database.
- [23] S. Bashkin and J. O. Stoner. *Astronomische Nachrichten*, 298(3):187–187, 1977.